浙 江 大 学

本 科 生 毕 业 论 文（设计）

题目　　低温原子力显微镜下的点接触实验

姓名与学号　　　靳岵　　3090000207

指导教师　　　危健　王浩华

年级与专业　　**2009** 级　　物理学专业

所在学院　　　竺可桢学院理工平台　　理学院物理系

浙江大学本科生毕业论文（设计）诚信承诺书

1.本人郑重地承诺所呈交的毕业论文（设计），是在指导教师的指导下严格按照学校和学院有关规定完成的。

2.本人在毕业论文（设计）中引用他人的观点和参考资料均加以注释和说明。

3. 本人承诺在毕业论文（设计）选题和研究内容过程中没有抄袭他人研究成果和伪造相关数据等行为。

4. 在毕业论文（设计）中对侵犯任何方面知识产权的行为，由本人承担相应的法律责任。

毕业论文（设计）作者签名：

_____年_____月_____日

本科生毕业论文（设计）任务书

一、题目：〰〰〰〰〰〰〰〰〰〰〰〰〰〰〰〰〰〰〰〰〰〰〰〰

二、指导教师对毕业论文（设计）的进度安排及任务要求：

　　　　　　　　　　　　起讫日期 **200** 　年　　月　　日 至 **200** 　年　　月　　日

　　　　　　　　　　　　　　　指导教师（签名）〰〰〰〰〰职称〰〰〰〰〰

三、系或研究所审核意见：

　　　　　　　　　　　　　　　负责人（签名）〰〰〰〰〰

　　　　　　　　　　　　　　　　　　年　　月　　日

Abstract

Point contact Andreev reflection spectroscopy (PCARS) has been widely applied to study the gap structure and order parameter symmetry of unconventional superconductors. We propose a method combining PCARS and shot noise measurements [1] to investigate equal spin triplet pairing and long-range coherent transport in superconductor/ferromagnet heterostructures.

We successfully established a PCARS setup based on an Attocube low-temperature atomic force microscope (AFM). High resolution of differential resistance measurements is achieved: structures with deviation of $\sim 1\%$ from the overall differential resistance could be clearly distinguished.

We obtained differential resistance curves of W-Ti/Au and W-YBCO point contacts. For W-Ti/Au point contacts, no structure is observed within the noise level. As to W-YBCO point contacts, a possible signature of gap structure is observed.

摘要

点接触 Andreev 反射谱作为一种实验手段已经被广泛应用于非常规超导体的能隙结构和配对对称性研究。我们提出一种将点接触 Andreev 反射谱和散粒噪声测量相结合的方法[1]，来研究超导/铁磁异质结中的同自旋自旋三态配对和长程相干输运现象。

我们成功搭建了一套点接触 Andreev 反射谱实验系统，这套系统基于 Attocube 公司的低温原子力显微镜。我们的微分电阻测量达到了很高的分辨率：相对于总体微分电阻变化在 $\sim 1\%$ 的结构可以被清楚地分辨。

我们测量了 W-Ti/Au 和 W-YBCO 点接触的微分电阻谱。对 W-Ti/Au 点接触，在噪声范围内我们没有观察到任何结构。对 W-YBCO 点接触，我们观察到了一个可能的能隙结构信号。

Acknowledgement

First, I would like to thank the people who made this work possible. Professor WEI Jian keeps providing supports using his rich experimental experiences and in-depth understanding of physics. Discussion with him is always enlightening. He encourages us to take the hands-on experiments independently and is always patient with our mistakes, which provides us with a precious environment to accumulate our own experiences and grow as a experimentalist. WANG He is my main collaborator, without whom this work will not even be possible. In particular, most of the work of tip and sample preparation is done by He. I would always thank his tolerance towards my willfulness. LIU Liang helped a lot with LabVIEW programs and wire bonding. ZHOU Bowen helped to take the SEM images of the tip. XU Fang taught me how to make Indium electrodes. I would thank all the group members in Professor WEI Jian's lab, including XIANG Li, for helpful discussions and beautiful memories of working together. Some other people in Peking University also contributes to this work. YANG Tao and WEI Yuke provided us with the YBCO sample. Professor WU Xiaosong provides GE Varnish. Discussions with Professor JIANG Ying and Professor ZHANG Zhaohui helped me get more knowledge of the AFM. The engineer from Attocube, Doctor Christian Debuschewitz, helped a lot with the AFM. Professor WANG Haohua gave me great assistances about undergraduate thesis affairs in the Physics Department of Zhejiang University.

Furthermore, since this is the acknowledgement of my undergraduate

pany and encouraged me to move forward.

Contents

List of Figures

List of Tables

Chapter 1

Introduction to point contact Andreev reflection spectroscopy (PCARS)

This chapter follows the approach in Section III of Ref [7].

1.1 Andreev reflection and point contacts

When an electron moving in a normal metal hits the interface with a superconductor, what will happen? If the kinetic energy of the electron measured from the Fermi level is bigger than the energy gap Δ of the superconductor, basically it will be transmitted as an electron-like quasi-particle to the superconductor. But if its kinetic energy is smaller than the energy gap Δ, this transmission cannot occur, since there are no available states within the energy gap. In 1964, A. Andreev proposed a process which is known as Andreev reflection taday [8]. In this mechanism, an electron from the normal metal with a kinetic energy smaller than the energy gap will bound with another electron in the normal metal, and both of them will be transmitted into the superconductor as a single Cooper pair. If we look at this process within the normal metal, every time when an electron penetrates through the interface into the superconductor, an additional hole with reversed effective mass, spin and velocity will be reflected from the interface, along the opposite direction of the initial electron trajectory. [9]

Since Andreev reflection is a direct effect of the superconducting energy gap, it is easily understood that a lot of information about the gap structure can be extracted from the Andreev reflection process. For experimental measurable quantities, Andreev reflection will have effects on both heat transport (thermal resistance) and electron transport (electronic resistance) through the normal-metal/superconductor (N/S) structure. Andreev was interested in heat transport in his original paper [8], while we care more about electron transport. To study the electron transport properties, the first idea one might come up with is to measure the I-V curve of the N/S structures. Further, to get a better knowledge of structures in an I-V curve, one might want to measure the differential resistance or differential conductance, or even higher derivatives of I(V), as a function of bias voltage V, of the N/S structure. This experimental method is called Andreev reflection spectroscopy (ARS). For reasons thoroughly explained in Ref [7], a small contact size between normal metal and superconductor is favorable for ARS experiments. The main reason is to get rid of heating effects at the contact area. Here "small" means that the radius a of the contact area is smaller than both the electronic mean free path and the coherent length of the superconductor. Experimentally this small contact is realized by employing the Sharvin contact or point contact method. ARS of an N/S point contact is called point contact Andreev reflection spectroscopy (PCARS).

A common method of fabricating point contacts is the needle-anvil method, in which a relatively sharp normal metal tip, having a local radius of curvature of the order of $1\mu m$, is carefully brought into contact with a flat bulk superconducting sample or a thin film. It turns out that in this kind of setup the radius of the contact area can usually satisfy the conditions mentioned above. [7]

PCARS has been an important tool to study unconventional superconductors, such as heavy fermions, high-T_c superconductors, iron-based superconductors, etc. [9] Results on high-T_c superconductors are reviewed in Ref

[7]. A recent result is the study of d-wave superconductivity in the heavy-fermion superconductor PuCoGa$_5$ [10]. Ref [10] includes a clear short introduction to PCARS and its application to investigate the gap structure and order parameter symmetry of superconductors.

1.2   Blonder-Tinkham-Klapwijk (BTK) model

The theory of electron transport at an N/S interface, with Andreev reflection taken into consideration, is completely discussed by G.E.Blonder, M.Tinkham and T.M.Klapwijk in 1982 [3], which is know as the BTK model. They also discussed the effect of an imperfect (not fully transparent) interface between the normal metal and the superconductor and developed a complete theory from metallic to tunneling regimes. They also successfully compared their theoretical predictions to experimental measurements performed on point contacts [11].

In Ref [11], a qualitative discussion of the BTK model was given, which is easily understood. We suppose that there is no Fermi level mismatch effect (which is actually equivalent to the effect of a larger effective Z parameter [11]) between the normal metal and the superconductor. If a voltage V is kept at the N/S ends, the maximum energy of electrons flowing from the normal metal to the superconductor will be eV. When the bias voltage $V < \Delta/e$, Andreev reflection will occur. If the electron carries ev_F of current, v_F being the Fermi velocity, then $2ev_F$ of net current is flowing, because the reflected hole carries $(-e)(-v_F)$. So the differential resistance will be half of that in normal state. When the bias voltage $V > \Delta/e$, as V increases, the fraction of electrons carrying twice the normal current, i.e. those Andreev reflected, decreases. When V is much greater than Δ/e, the differential resistance will be the same as that in normal state. So the differential conductance as a function of bias voltage will be like that in the top-left figure of Fig 1.1. This is the case when $Z = 0$, i.e. there is no

potential barrier at the interface, which is called the pure metallic case. If $Z > 0$, there will be other phenomena occurring. Fig 1.1 shows the theoretical differential conductance curves at different Z values. Especially, if a potential barrier is present, the conductance presents two maxima at voltages approximately $\pm\Delta/e$ and a zero-bias minimum [10].
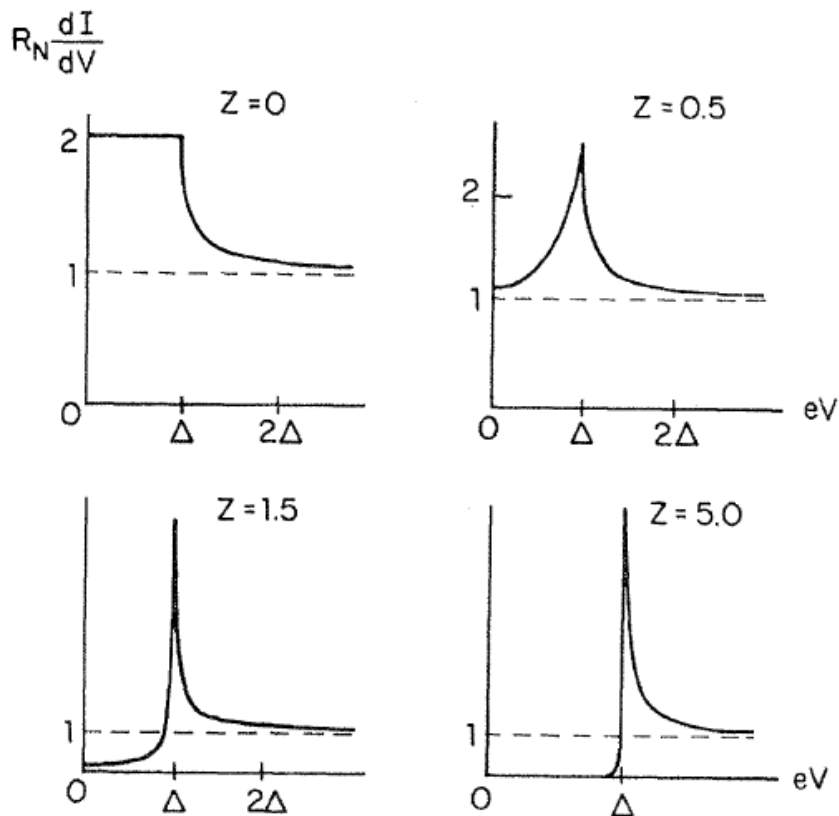
Figure 1.1: Figure taken from Ref [3]. Differential conductance vs voltage for various barrier strengths Z at T=0. The Z=0 case is the pure metallic case.

The BTK model is only one-dimensional. For three-dimensional N/S systems, it is still a good model as long as the superconducting gap is isotropic [9]. Extensions of the BTK model to two- and three-dimensions and superconductors with different order parameter symmetries have been established. If we compare the results of a PCARS experiment with theoretical predictions, we'll get knowledge of the gap structure and order parameter

symmetry of a superconductor. Ref [10] is an example of this.

1.3   More about PCARS and point contacts

1.3.1   PCARS of superconductor/ferromagnet structures

In previous discussions we restrict ourselves to N/S structures, where rich interesting physics have already emerged. If we broaden our insight into more complicated structures, with a superconducting layer always existing, even more phenomena will occur. Superconductor/ferromagnet (S/F) structure is such an example which has drawn a lot of attention [12][13]. A dedicated chapter on a specific phenomena in S/F structures will be given later. Here we only mention an application of PCARS in S/F structures, i.e. to measure the spin polarization of a metal [14]. In an S/F interface, unlike in the case of S/N interface, Andreev reflection will be suppressed due to spin polarization of the ferromagnet. The effect is that the enhancement of differential conductance relative to the value at normal state will be less than 2 in the metallic regime. R.J.Soulen et al were able to make use of this effect to determine the spin polarization of a metal [14].

Since the Andreev reflected hole has both opposite charge and spin to the incident electron, one might think that both spin and charge will contribute to measurable effects in this process. In N/S structures, only the charge effect is paid attention to, while the spin effect is rarely mentioned. The application of PCARS in S/F structures might remind us of the spin effect in Andreev reflection. And more applications of this spin effect may appear.

1.3.2   Point contact as a test-bed for quantum electronic transport [2]

Point contact is not only used for PCARS experiments, it's also a test-bed for quantum electronic transport. If the radius W of the point contact area is sufficiently small and is comparable to the Fermi wave length λ_F of the electron (Such a point contact is called a quantum point contact), the point contact neck could be considered as a wave guide, while the electron transported through the neck could be considered as electromagnetic waves. Thus only a small integer number $N \approx 2W/\lambda_F$ of transverse modes can propagate at the Fermi level. It turns out that each of these modes carries the same current Ve^2/h, where V is the bias voltage and h is the Plank constant. Summing over all modes in the wave guide, the conductance of the point contact would be $G = Ne^2/h$. If we continuously change the contact size W, only integer number of modes will be generated or annihilated. Thus the conductance will be quantized to a step size e^2/h. Experimentally the step size will be $2e^2/h$ because of the degeneration of spin-up and spin-down modes. It's difficult to observe such a conductance quantization in normal metal quantum point contacts because λ_F is extremely small ($\sim 0.5nm$) for a normal metal. The 2D electron gas in a GaAs-AlGaAs heterojunction has a Fermi wave length much larger than that, where conductance quantization has been observed. [2]

Quantum point contacts are closely related to some of the hot topics in current condensed matter research, such as Quantum Hall Effect and Majorana Fermions. In particular, a method has been proposed to detect Majorana Fermions by coupling a topological superconductor with a normal-metal quantum point contact [15][16].

Chapter 2

Equal spin triplet pairing and long-range coherent transport in superconductor/ferromagnet heterostructures

2.1 From SIS to SNS to SFS

Consider a Josephson junction, i.e. two superconducting (SC) layers with a thin insulating layer in between (SIS structure). There will be couplings between Cooper pair wave functions in the two SC layers, which result in Cooper pair tunneling from one of the SC layers to the other. And there will be a dc Josephson current even if the bias voltage is zero. This effect requires that the thickness of the insolating layer must be small, otherwise the coupling of the two superconducting layers will be too small to induce detectable Josephson current.

If the insulating layer in a Josephson junction is replaced by a normal metal layer (SNS structure), Andreev reflection at the normal-metal and superdconductor interface will induce proximity effects. In the SC layer, the SC wave function is suppressed over the correlation length ξ_s, while in the normal metal layer, the SC condensate penetrates into the normal metal over

the length ξ_N, which could be $\sim \mu m$ at low temperature. Fig 2.1 shows the pair potential (or SC gap or SC order parameter) in an SNS structure. Due to this effect, the normal metal layer could be relatively thick while the two SC layers still couple with each other. [17]
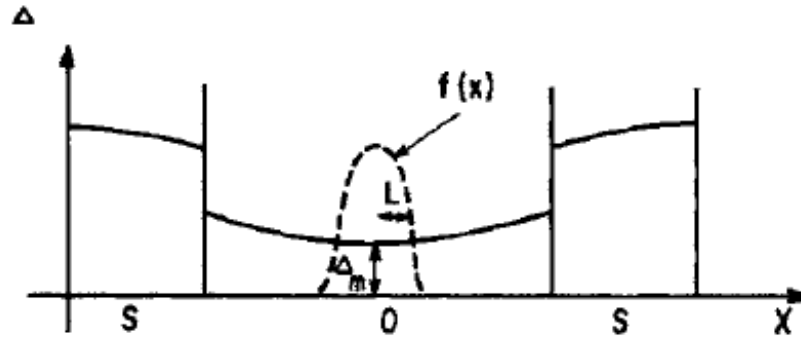
Figure 2.1: Figure taken from Ref [4]. Spatial dependence of the pair potential at temperatures close to the transition point in an SNS junction. We ignore the f(x) curve.
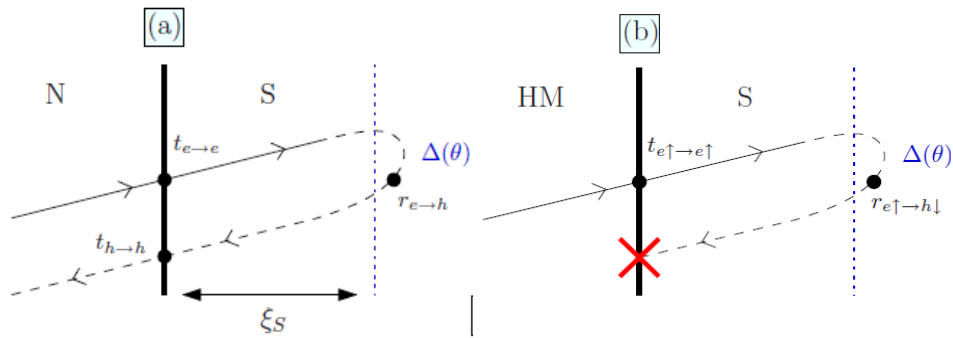
Figure 2.2: Figure taken from Ref [5]. Andreev reflection scattering at (a) NS interface and (b) HM/S interface. HM could be considered as a 100% spin-polarized ferromagnet.

If we further replace the normal metal layer by a ferromagnetic layer (SFS structure), and suppose that the Cooper pair in the SC layer is spin singlet, the probability of Andreev reflection will be suppressed. The reason is that Andreev reflection requires that the reflected hole has an opposite spin to the spin of the incident electron. But in a ferromagnet, the density

of states of the spin-minority states at the Fermi level is extremely reduced. And in the 100% spin-polarization case, as in half-metals (HM), there is no available states for the reflected hole, thus there will be no possibility of Andreev reflection. See Fig 2.2. The result will be that the conventional proximity effect is suppressed in an SFS junction. The coherent length ξ_F will be only ∼nm or shorter. [18][5]

2.2   Equal spin triplet pairing and long range coherent transport in SF structures

If the ferromagnet in an SF structure is not 100% spin-polarized, there will be Cooper pairs diffusing from the SC layer to the ferromagnetic layer. Suppose that the Cooper pair in the SC layer is spin-singlet ($\uparrow\downarrow - \downarrow\uparrow$). Cooper pairs diffusing into the ferromagnet will be transformed to a mixed state of spin-singlet state ($\uparrow\downarrow - \downarrow\uparrow$) and spin-triplet state ($\uparrow\downarrow + \downarrow\uparrow$) due to existence of strong exchange field in the ferromagnet [6][5]. This is called spin-mixing. But this mixed pair amplitude will still be suppressed quickly in the ferromagnet by the exchange field. Because both the ($\uparrow\downarrow - \downarrow\uparrow$) state and the ($\uparrow\downarrow + \downarrow\uparrow$) state are not spin-polarized, which will not survive in the spin-polarized ferromagnet [6]. See the left figure of Fig 2.3.

So how to make the pair amplitude long survive in the ferromagnet of an SF structure? The solution is to create pair amplitude components $\uparrow\uparrow$ or $\downarrow\downarrow$, which are spin-polarized and could survive in the existence of the exchange field. These two states are called equal spin triplet states. Note that the three triplet states transform into each other when the quantization direction changes, e.g. the ($\uparrow\downarrow + \downarrow\uparrow$) triplet state in the y-basis is the equal spin $i(\uparrow\uparrow + \downarrow\downarrow)$ triplet state in the z-basis. So if there is an interface layer between the SC layer and the ferromagnetic layer, which is magnetized in a different direction with the ferromagnetic layer, the ($\uparrow\downarrow + \downarrow\uparrow$) state induced from spin-mixing will result in equal spin triplet states. This is called

spin-flip. And this equal spin triplet pairing can be coherently long-range transported in the ferromagnet [6]. See the top-right figure of Fig 2.3. This interface layer is usually a ferromagnetic domain wall in a real experimental system. In an SFS structure, if there are interface barriers at the two SF interfaces, depending on the relative magnetic orientations of the two interface regions, a 0-junction or a π-junction can be prepared, which will find its industrial applications [6]. See the bottom-right figure of Fig 2.3.
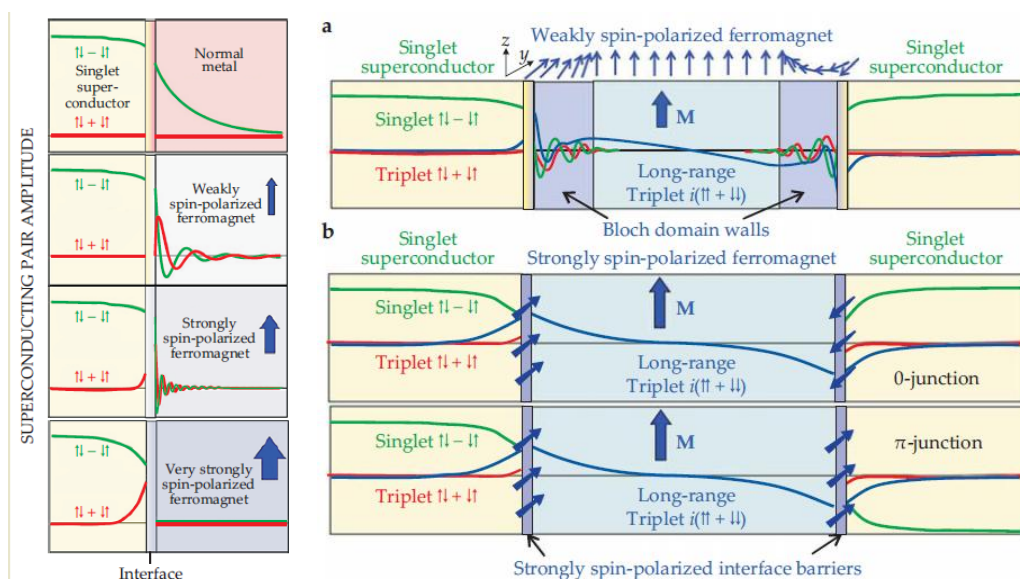
Figure 2.3: Figure taken from Ref [6]. Left: Spin-mixing and suppression of the pair amplitude by the exchange field. Top-right: Spin-flip and long-range triplet supercurrent. Bottom-right: 0-junction and π-junction prepared using the long-range triplet supercurrent.

Chapter 3

Proposal

3.1 Previous results

The equal spin triplet pairing and long-range coherent transport in SF structures have not been conclusively confirmed in experiments. Some of the previous results are as follows.

- STM study on LCMO/c-axis YBCO bilayer: no SC gap or zero-biased conductance peak (ZBCP) observed for junctions with LCMO layer of even 5nm. This suggests that only spin-singlet pairing exists in LCMO, which is significantly suppressed by exchange field in LCMO. [19]

- STM study on LCMO/a-axis YBCO bilayer: SC gap and ZBCP observed for junctions with LCMO layer of up to 30nm. This suggests that equal-spin triplet supercurrent exists in LCMO. [20]

- McMillan-Rowell resonances observed in the differential conductance of c-axis YBCO/LCMO bilayer and YBCO/LCMO/YBCO trilayer. This suggests the existance of equal spin Andreev reflection in the S/F interface and equal-spin triplet supercurrent. [18]

3.2   Proposal: combination of PCARS and shot noise measurements

The key point is to determine the order parameter symmetry in the ferromagnet of the SF structure. Information from STM experiments are difficult to analyse, due to various contributions to the structures in differential conductance curve. Ref [21] shows that shot noise measurements of superconductor/normal-metal junction should show different behavior depending on the order parameter symmetry of the superconductor. Ref [22] further shows this difference in superconductor/normal-metal point contacts. So we believe that PCARS is a more powerful tool to investigate this subject, especially when combined with shot noise measurements [1]. On the one hand, PCARS, unlike STM, which is always a tunneling junction, is in a relatively clean ballistic transport regime, so that the effect of Andreev reflection will not be totally concealed. Considering that Andreev reflection is directly related to the order parameter symmetry, PCARS is born to be a better tool to investigate the order parameter symmetry than STM. On the other hand, PCARS could be easily combined with shot noise measurements, which will give us much more information about the order parameter symmetry. It should be noted that point contact spectroscopy has been used to study the non-monotonic behavior of the superconducting order parameter in SF structures [23].

Chapter 4

Experimental setup

4.1 Overall configuration of the experimental setup

We developed a PCARS experimental setup based on an Attocube tuning-fork (TF) atomic force microscope (AFM) system. Figure 4.1 shows the overall configuration. The setup is mainly composed of three parts.

- The AFM probe with a needle-anvil type point contact built in. When running the experiment, this probe will be inserted in a cryostat, for instance, a dilution fridge, or simpler, a liquid nitrogen dewar or a liquid helium dewar.

- The AFM controlling system. This system provides precise control of the piezo positioners and scanners. The system is developed by Attocube.

- The differential resistance measurement setup (DRMS). We employ a standard dc+ac lock-in method to measure the differential resistance of the point contact, in order to obtain the PCARS. This is the electronic circuit we built for the measurements.

Details of every part of the setup will be described in the following sections.
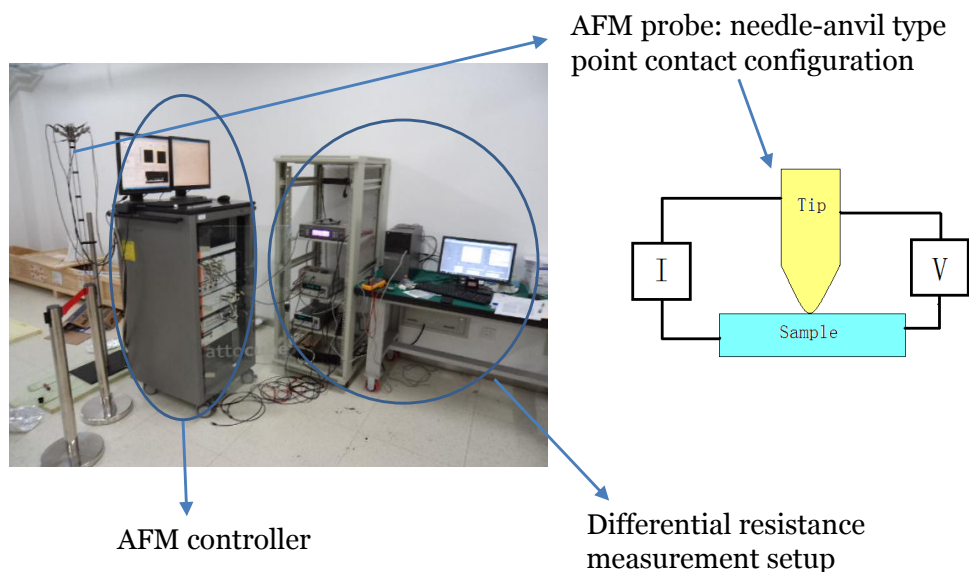
Figure 4.1: The overall configuration of our experimental setup for PCARS. The right figure shows the needle-anvil type point contact.

4.2 The atomic force microscope

In point contact experiments, the AFM is only used for precisely moving the sample and its capability is not made the best of. Previously all the piezo positioners and scanners we were using are from Attocube, although they are not made by Attocube. These positioners and scanners are extremely delicate and easily broken, especially the z-scanner. After breaking the z-scanner twice, we decided to replace the z-scanner from Attocube by one made from another company. (We'll call these two the Attocube z-scanner and the homemade z-scanner respectively.) In order to check whether the homemade z-scanner can well fit the Attocube system, we need to know how long the piezo will elongate under some specific applied voltage, and compare it with the Attocube z-scanner. In this section we'll discuss results related to this purpose.

We know that in a standard AFM scanning process, the voltage applied

to the z-scanner is set to be 0-60V. And if a maximum 60V voltage is applied to the z-scanner, the program will set the height of the detected structure to z max. range, a value which could be manually set in the program. If we use a standard grating sample and compare the measured result with the real height of the structures, we'll get knowledge of elongation of the z-scanner.
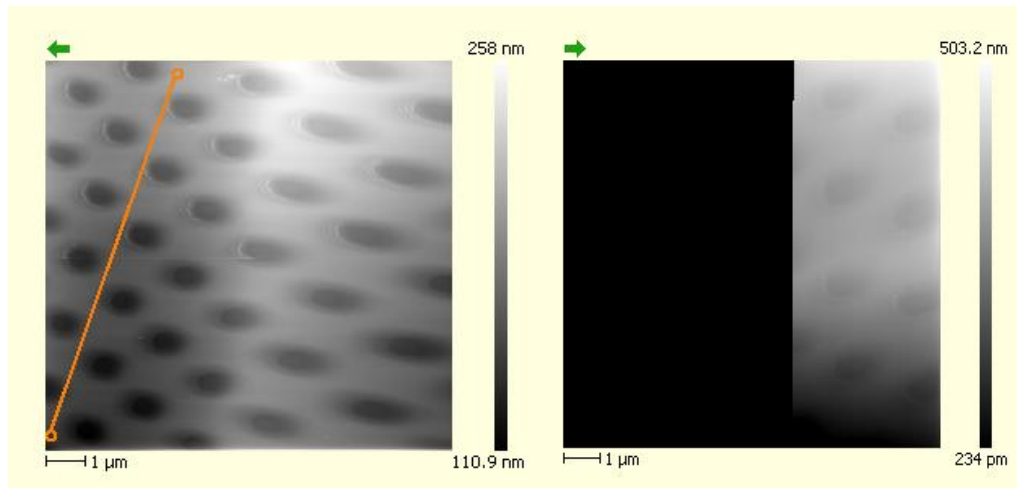
Figure 4.2: AFM images of a standard grating sample. For determination of the elongation of the homemade piezo z-scanner.
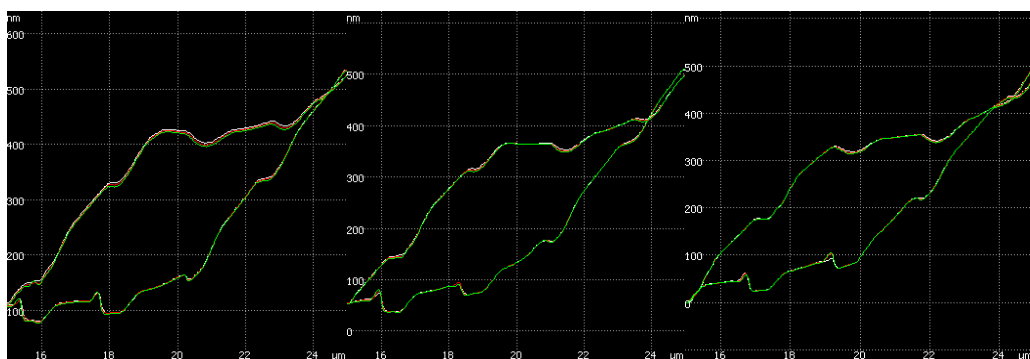
Figure 4.3: Three groups of raw data of line views when scanning a standard grating sample. For determination of the elongation of the homemade piezo z-scanner.

Fig 4.2 shows AFM images of the standard grating sample. The right figure is a scanning along the direction of the orange line in the left figure.

The z max. range is set to $2\mu m$. Scanning is along vertical lines in the right figure of Fig 4.2. Fig 4.3 shows three groups of line views along this direction. We use these three groups of data to determine the measured depth of the round spots in the standard grating sample. The nominal depth of the round spots is 20nm. Data processing is as follows. Each group of data consists of three times back and forth scanning, we first take the average of them and only use, say, the forth scanning data. Then we subtract the background from the data, as shown in the top-left figure in Fig 4.4. Finally we get data shown in Fig 4.4 (except top-left). Now we can easily read out the depth of each spots. The average depth turns out to be 28.0nm. So the real elongation of the homemade z-scanner under a voltage of 60V is $\frac{20\text{nm}}{28\text{nm}} \times 2\mu m \approx 1.4\mu m$.
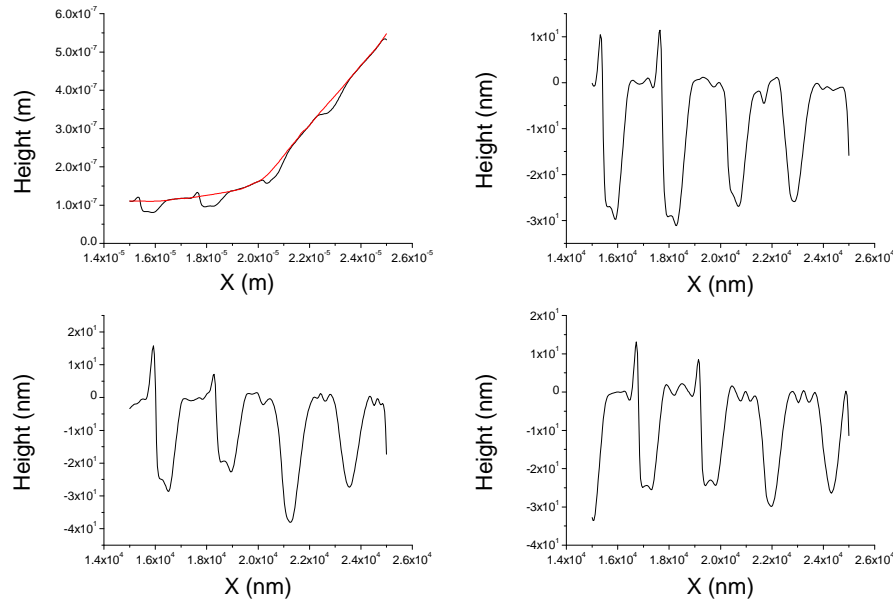
Figure 4.4: Data processing of the line-view data of scanning a standard grating sample. For determination of the elongation of the homemade piezo z-scanner. For details, see text.

Fig 4.5 shows a similar result for the Attocube z-scanner. The measured depth is about 16nm, while the nominal depth is 20nm. So the real elongation of the Attocube z-scanner under 60V voltage is $\frac{20\text{nm}}{16\text{nm}} \times 2\mu m =$

$2.5\mu m$. In conclusion, although the elongation of the homemade z-scanner is about half of that of the Attocube z-scanner, the homemade z-scanner can still fit the Attocube system. After all, differences between the two z-scanners are not as big as we previously expected.
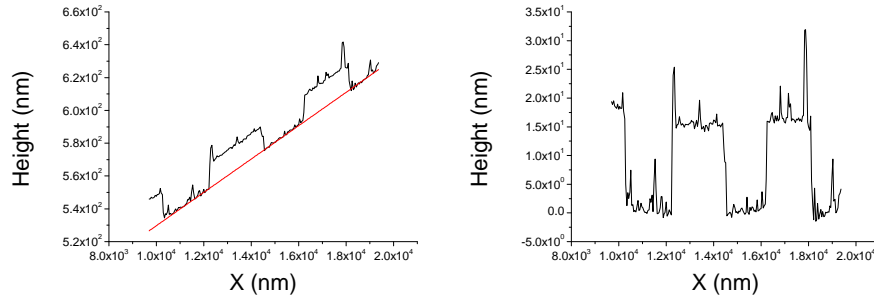
Figure 4.5: Data processing of the line-view data of scanning a standard grating sample. For determination of the elongation of the Attocube piezo z-scanner. For details, see text.

4.3   Differential resistance measurement setup

We employ a standard dc+ac lock-in method to measure differential resistance (or differential conductance). Fig 4.6 is an enlarged picture of DRMS. The principle is as follows [24]. In a typical I-V measurement, the device under test (DUT) is supplied with a direct current I; and the voltage drop on the DUT is measured. If we sweep the dc current I, an I-V curve will be obtained. In order to measure the differential resistance, the DUT is supplied with a definite frequency ω ac current, besides the dc current I. Now the voltage drop on the DUT, as a function of dc+ac current, can be

presented as a Taylor series

$$
\begin{aligned}
V(I + i\cos(\omega t)) &= V(I) + \frac{dV}{dI} i\cos(\omega t) + \frac{1}{2}\frac{d^2V}{dI^2} i^2 \cos^2(\omega t) + \cdots \\
&= V(I) + \frac{dV}{dI} i\cos(\omega t) + \frac{1}{4}\frac{d^2V}{dI^2} i^2 (1 + \cos(2\omega t)) + \cdots
\end{aligned}
$$

$$(4.3.1)$$
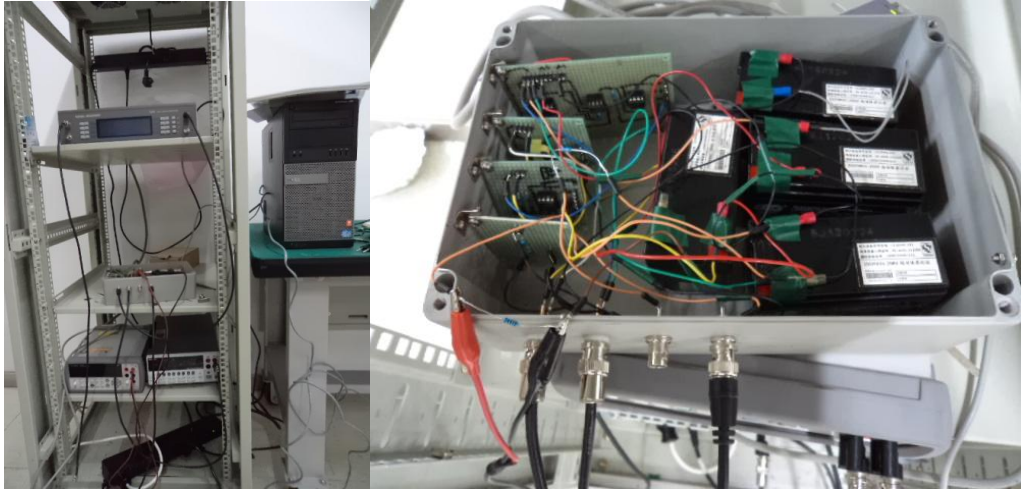
Figure 4.6: Enlarged picture of the differential resistance measurement setup.

If the ac current amplitude i is small enough, the higher order terms in Equation 4.3.1 can be neglected. And if we measure the voltage drop on the DUT at the specific frequency ω, the measured signal will be proportional to the first derivative of $V(I)$, i.e. the differential resistance $\frac{dV}{dI}$. This measurement is achieved by a lock-in amplifier, which is specially designed to pick up small ac signals at some specific frequency from an overwhelming noise background. We also measure the direct voltage drop on the DUT at the same time. Then when we sweep the dc current, a $\frac{dV}{dI}$ vs V curve will be obtained. It should be noted that the same method can be used to measure the second derivative $\frac{d^2V}{dI^2}$. We only need to adjust the lock-in amplifier so

that it could pick the signal at frequency 2ω, as easily seen from Equation 4.3.1.

The method described above is actually called the current-bias method. An alternative way is to supply a dc+ac voltage to the DUT and use a lock-in amplifier to measure the current at frequency ω through the DUT, which is called the voltage-bias method. In this way, we will obtain a $\frac{dI}{dV}$ vs V curve instead of a $\frac{dV}{dI}$ vs V one. In another word, we are measuring the differential conductance instead of differential resistance. The reason is that, for the voltage-bias method, the function $V(I+i\cos(\omega t))$ in Equation 4.3.1 should be replaced by $I(V + v\cos(\omega t))$.

The two methods discussed above can be easily switched using the same circuit. Generally we use dc and ac voltage sources to excite the circuit. Thus the DRMS is actually born to be a voltage-biased circuit. In order to make the output voltage of the circuit (i.e. the voltage supplied to the DUT) constant, a voltage divider should be employed, in which a relatively small resistor is connected in parallel with the DUT, so that resistance change of DUT will not cause a significant change in the divider ratio. This configuration requires that the DUT should have a relatively large resistance for a voltage-biased measurement.

If we replace the voltage divider by a large resistor R_{v2i}, which is directly connected to the output of the circuit, then the dc+ac voltage source will be transformed into a dc+ac current source. Similarly, in a current-biased measurement, the DUT should have a relatively small resistance, so that the current is mainly determined by the resistor R_{v2i}.

In fact, these restrictions on the resistance of DUT for the two methods are not that crucial. In any rate, we will directly measure the dc voltage drop on the DUT in a real experiment. The restrictions will only guarantee that a linear dc voltage sweep of source-meters is transformed to a nearly linear dc voltage or current sweep on the DUT.

4.3.1   The circuit

Fig 4.7 is the diagram of our complete circuit for DRMS, with a lot of help from Ref [25][26][27]. The whole circuit is put in an aluminum box, to prevent the influence of environmental noises. There are basically three parts in the circuit, each of which is developed on a separate PCB, as shown in Fig 4.6.
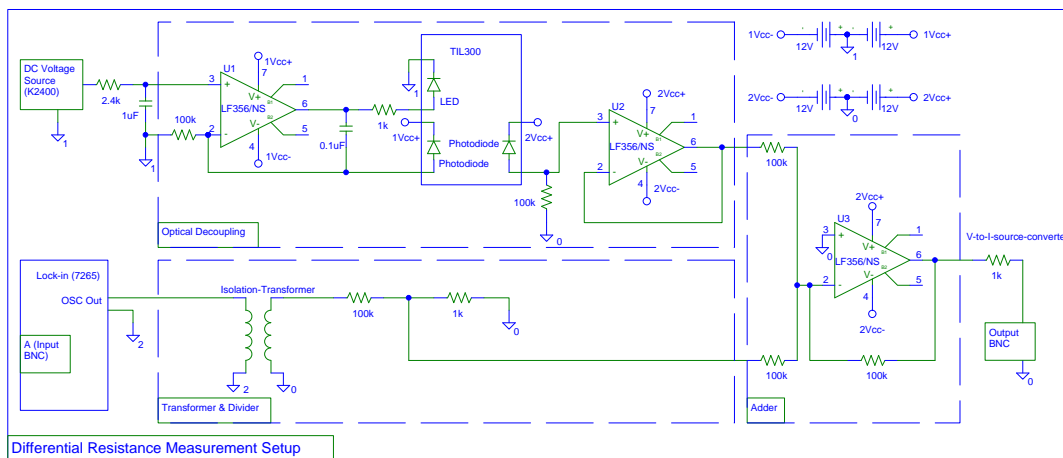
Figure 4.7: The complete circuit diagram of DRMS.

- Optical decoupling, to decouple the dc voltage source with the post-stage circuit. The main component of this part is a precision linear analog opto-isolator TIL300 (TAOS). Since in the opto-isolator, LED and photodiode are not electronically connected, the grounds of front- and post-stage circuit can be isolated. This part is the standard circuit suggested in the data sheet of TIL300. We will call this part the TIL300 circuit hereinafter.

- Transformer and voltage divider, to decouple the ac voltage source with the post-stage circuit. An audio-frequency isolation transformer is used, whose primary coil and secondary coil are not commonly grounded.

- Adder, to add the ac and dc voltage together and supply it to the DUT.

A resistor $R_{v2i} = 1k\Omega$ is connected to the output of the adder, to convert the voltage source to a current source. If we need a voltage-biased measurement, simply replace R_{v2i} by a voltage divider.

DC source voltage is supplied by Keithley 2400 SourceMeter, while ac source voltage is supplied by a Signal Recovery 7265 lock-in amplifier, which is also used for ac signal measurement.

There are totally two ports in DRMS (shown in Fig 4.7), the output BNC and the input BNC, which is also the A input port of 7265. For a current-biased measurement, simply figure out a way to connect the DUT between the output BNC and the input BNC. Some adjustments should be employed for a voltage-biased measurement.

We also developed LabVIEW programs for controlling and data-acquisition, and for various experimental purposes.

4.3.2   Some basic tests of the circuit

After finishing the DRMS establishment, we first carried out some basic tests of the circuit, to make sure it can work well.

The transformer

The transformer we used is not a standard device and we've got no data sheet for it. To understand its behavior, we supply a 0.1V ac voltage, of different frequencies, to the primary coil, and measure the voltage signal after the transformer and a 1:100 voltage divider. If the transformer ratio is 1:1, as is claimed, then the voltage measured should be 0.99mV. The test is achieved by a 7265 lock-in amplifier. Results are shown in Fig 4.8

It can be seen that if we want the transformer to work in its ratio 1:1 regime, we should use an ac signal of frequency above 23Hz. (At 23Hz, the

output is 90% of 0.99mV) We can also see that the signal passing through the transformer will gain an extra phase of π, which is not relevant.

Note: Another property of the transformer should also be checked. That is to measure the output of the transformer when the input is supplied with an ac voltage of some definite frequency, but of different amplitudes. We did not pay attention to this property at first. But it turned out to be an important one. Because when the input amplitude is relatively large, the second coil of the transformer may fail to supply a sufficiently large power to keep its 1:1 ratio. Anyway, we will not change the amplitude or frequency of the ac excitation frequently in a real experiment. They will be kept constant in one experimental run. Thus we do not require a linear response of the transformer to amplitude or frequency changes.
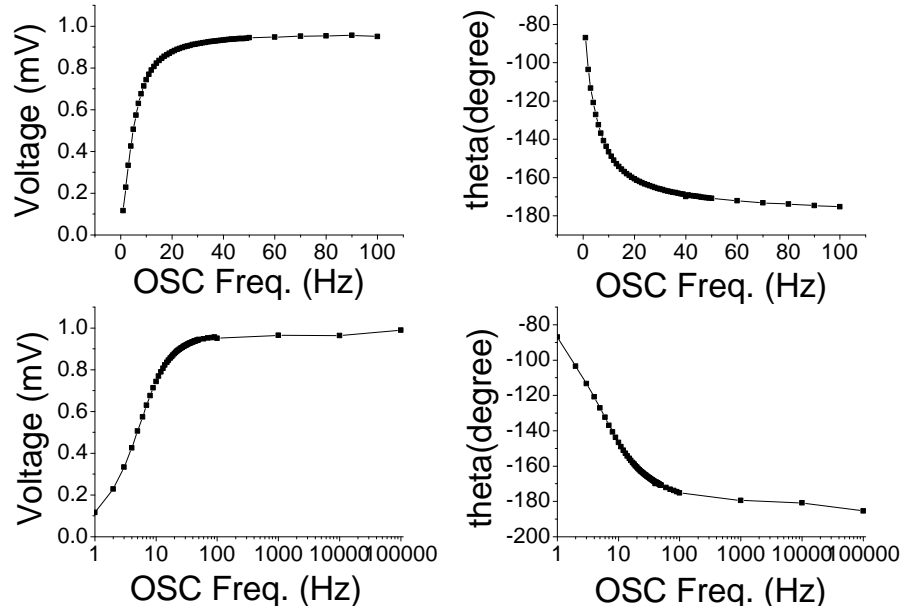
Figure 4.8: Properties of the isolation transformer in DRMS. For all of the four figures, voltage supplied to the primary coil is kept constant. Top-left: amplitude of the output voltage as a function of frequency; Top-right: phase change of the output signal relative to the input signal as a function of frequency. Bottom-left/right: the same as top-left/right respectively, x-axis changed to log scale.

The optical decoupling

It is significant that the output voltage responds linearly to the input voltage of the optical decoupling. Because when we are employing a linear sweep at the input, supplied by the dc voltage source-meter 2400, we hope that the output is also a linear sweep, at least in some voltage ranges. So we carried out the following test. We use a 2400 to supply an input dc voltage to the optical decoupling, at different values; and use a Agilent 34410A digital multimeter to measure the output dc voltage. The results are shown in Fig 4.9.

Figure 4.9: Properties of the optical decoupling in DRMS. Output voltage as a function of input voltage. Insets show enlarged figures of the low- and high-voltage regions.

It can be seen that, basically, the output voltage is proportional to the input at input voltages ranging from approximately 0.08V to 12.5V. But it's not a 1:1 transformation, although it should be 1:1 according to Ref [28]. Also, at input voltages above 12.5V, the output keeps constant in spite of changes of the input voltage. This is easily understood. The op-amps in

the TIL300 circuit are supplied by $\sim \pm 12V$ batteries and an op-amp cannot supply an output larger than the battery voltage. Furthermore, at input voltages below 0.08V, there are some weird behaviors. Fig 4.10 is a more careful measurement of the low-voltage region.
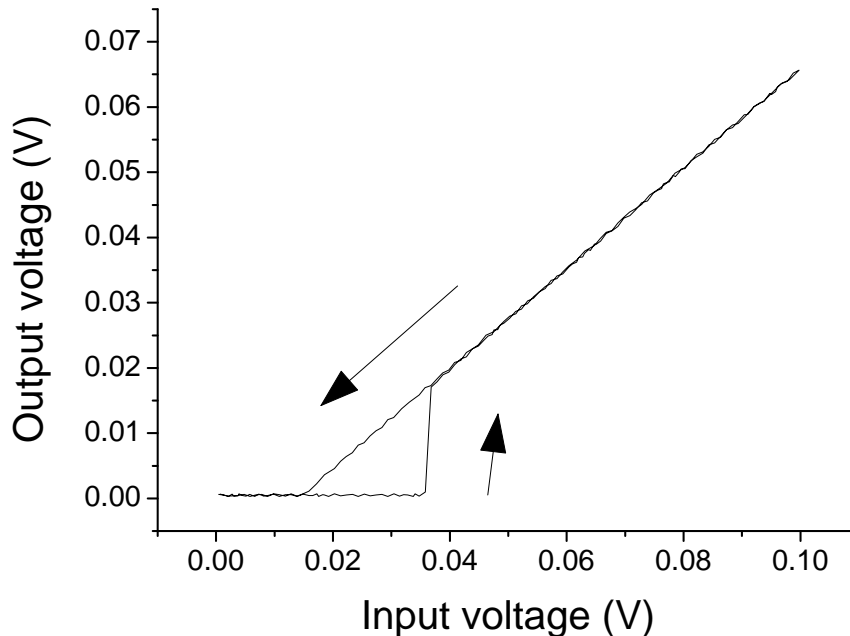
Figure 4.10: Properties of the optical decoupling in DRMS. Output voltage as a function of input voltage. A more careful measurement at low-voltage region.

When we are increasing the input voltage from zero, at first the output keeps zero and does not respond to the input. After we pass some kind of turn-on voltage of approximately 0.04V, the output keeps proportional to the input. Then when we are decreasing the input voltage from some value above the turn-on voltage to zero, no similar behaviors are observed. The reason for this behavior is not clear. It might be due to the LED or photodiodes in TIL300. After all, we can always avoid this weird region. If we need a small voltage at the output, we can simply add a voltage divider and keep the input at some safe values.

In Fig 4.11 we fit the linear region of Fig 4.9 to a straight line. The

fitted curve is

$$\text{Output voltage (V)} = 0.77738 \times \text{Input voltage (V)} - 0.04299\text{V} \quad (4.3.2)$$

This result depends on the battery voltage. So each time before we carry out a new experiment, we need to take this test to transform the input voltage to the output voltage. Although we'll be measuring the dc voltage drop on the DUT directly, it's a good idea to get the knowledge of this transformation before the experimental run.
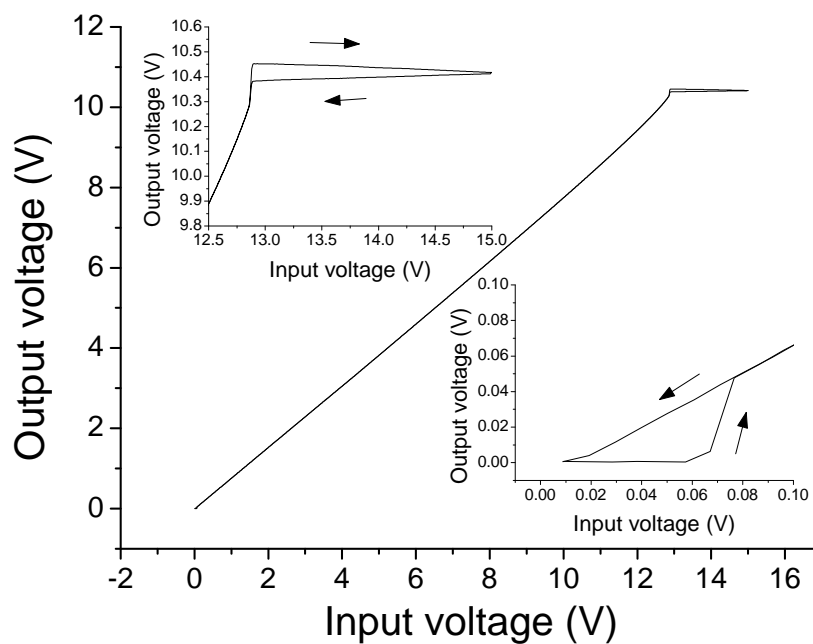

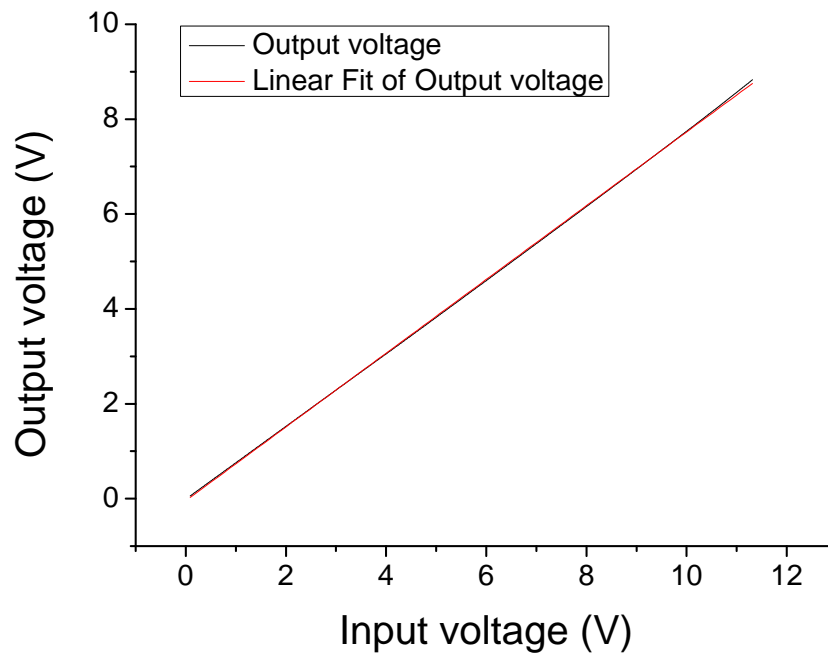Figure 4.11: Properties of the optical decoupling in DRMS. Output voltage as a function of input voltage. Linear region. Black curve is the experimental result. Red curve is the linear fit of it.

The adder

Some simple tests of the adder were carried out. We supply an ac voltage as well as a dc voltage to the input of the adder, and measure the dc and ac output of it. Results are shown in Table 4.1. An ac voltage of 0.1V and

100Hz is supplied to the input of the isolation transformer. We can see that the adder works well. And the signal passing through the adder will gain an extra phase of π, which is not relevant.

Table 4.1: Test results of the adder in DRMS

Input DC voltage/V	AC voltage after the voltage divider		AC voltage after the adder		DC after the adder/V
	Voltage/mV	Theta/degree	Voltage/mV	Theta/degree	
0.1	0.97	-174	0.96	5	-98.8 mV
0.2	0.96	-174	0.96	5	-0.199
0.3	0.96	-174.5	0.95	5.5	-0.299

4.3.3 How to make the readout of 7265 more stable?

When we were conducting tests on resistors and LEDs, we found it difficult to make the readout of 7265 sufficiently stable. It turns out there are two reasons for this difficulty. The first one is related to the circuit design. For example, if there are ground loops, the readout will be noisy. At first we just used a buffer instead of the optical decoupling and the result is not that satisfactory. The other reason should be attributed to the settings of 7265. After carefully reading the Handbook of 7265 [29], we found the following four factors that could have affected the readout.

- *In the current measuring mode, the input impedance is low (typically less than 100Ω), although it does rise as the operating frequency increases. If the very best performance is needed, then it may be better to use a separate dedicated current preamplifier.* [29] – Perhaps finally we need a current preamplifier or 1211 to convert small current to a large voltage. (7265 itself uses a I-to-V converter for current input mode: high bandwidth mode: 10^6 V/A, low noise mode: 10^8 V/A)

- *It is a basic property of the digital lock-in amplifier that the best demodulator performance is obtained by presenting as large a signal as possible to the main ADC. Therefore, in principle, the AC gain setting is made as large as possible without causing amplifier or converter overload.* [29] – So we need to always set the AC Gain as large as possible without making the input of 7265 overload. There is an option of automatic AC Gain setting, but it turns out that it fails to work well. Sometimes the input is already overloaded but 7265 fails to lower the AC Gain automatically.

- Sample rate. Following the anti-alias filter the signal passes to the main ADC which digitizes the input signal at the sampling rate ~ 166 kHz. It is supposed that the ADC will adjust its sampling rate around ~ 166 kHz according to the input signal. But if this automatic adjusting fails, a manual setting is needed. The sampling rate could be set to a 2% or 4% deviation of ~ 166 kHz. [29]

- Time constant. Controlling the time constant is equivalent to controlling the bandwidth of output low-pass filter. A larger time constant gives a smaller bandwidth, so that the output DC signal will be cleaner. Considering that the output of PSD will be a DC signal plus an AC signal of 2 times of the reference frequency (not including noises), when the reference frequency is small, a large time constant is needed. BTW, a single RC filter requires about 5 time constants to settle to its final value. [29]

After some trials, we found that the first three factors do not influence much on the readout, while the last one, i.e. the Time Constant, is indeed an important factor. My experience is to wait at least 8 time constants between two successive data-acquisition points. And the time constant itself should be adjusted to the ac frequency. For frequencies ~ 100Hz, the time constant should be at least 500ms.

4.3.4   Differential conductance measurements of a resistor

After carrying out the basic tests of the circuit mentioned above, we make sure that we have a good knowledge of every part of the circuit and that every part is working well. Then we continue to try differential conductance measurements using the circuit. We first test on a simple 1k resistor. We employ the voltage-bias method here. Results are shown in Fig 4.12. In Fig 4.12, the red points and black points are data points taken on a measurement where the dc voltage is supplied to the DUT through a 1k-10Ω voltage divider. The blue points are taken on a measurement where the DC voltage is supplied to the DUT through the adder directly. It can be seen that at lower bias voltages, the measured differential conductance is exactly as expected, i.e. $\sim 1/1k\Omega$. But at higher bias voltages, the data points abruptly drop to zero. This behavior might be due to the saturation of the op-amp, although it seems that the saturation behavior should not have occurred at such a small bias voltage. No further tests were carried out at that time. So I cannot give a clear explanation of it.
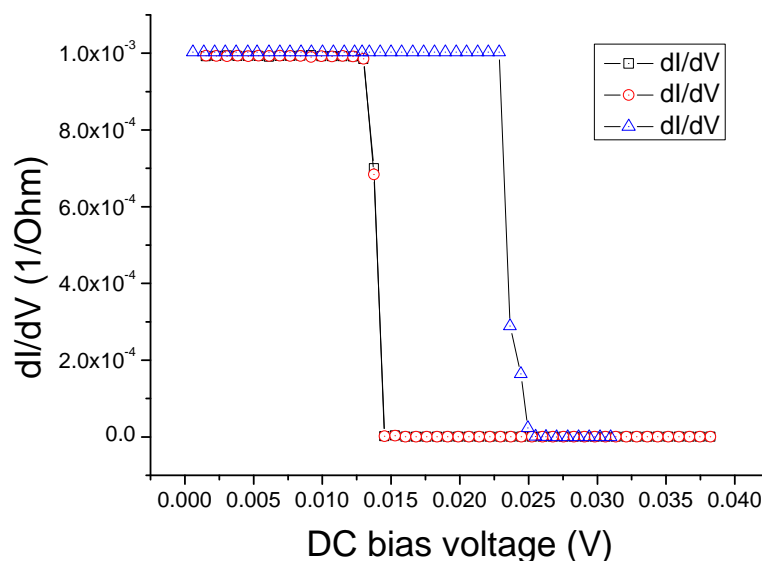

Figure 4.12: Results of differential conductance measurements of a 1k resistor. For details, see text.

4.3.5   Differential conductance measurements of an LED

We continue to try differential conductance measurements on an LED. We first measured the I-V curve of an LED, as shown in Fig 4.13. We only care about the forward region here. The right figure of Fig 4.14 shows the result of differential conductance measurements. The LED is connected directly to the output of the adder. The ac voltage source is of 0.1V amplitude and 77Hz frequency, which is supplied to the primary coil of the isolation transformer. And the ac voltage measured at the output of the adder is 956μV. The left figure of Fig 4.14 is the dc voltage drop on the LED as a function of dc voltage supplied to the input of the TIL300 circuit, which is measured simultaneously with the differential conductance. Comparison of the two figures in Fig 4.14 indicates that the abrupt drop in differential conductance result at dc bias ~ 1.6V is due to saturation of the op-amp.
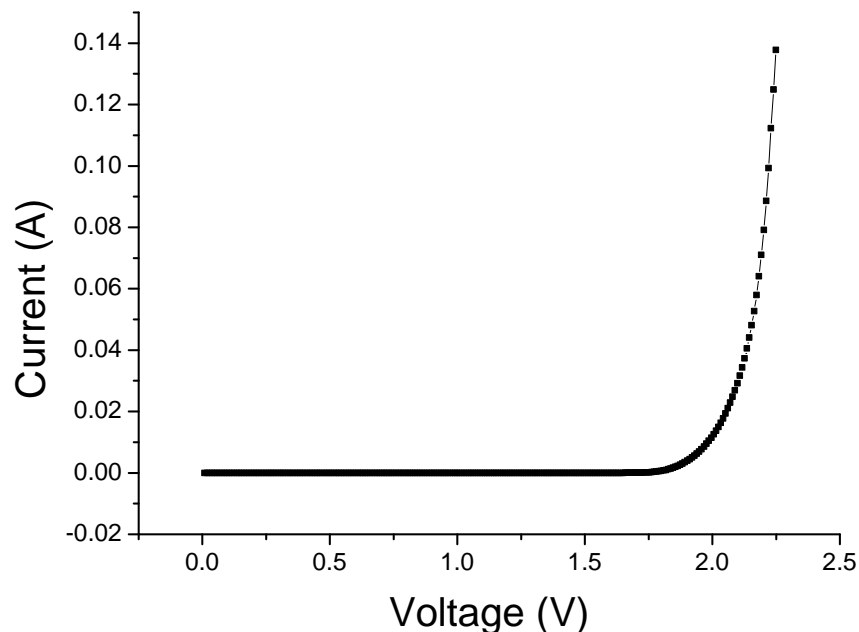

Figure 4.13: I-V curve of an LED.
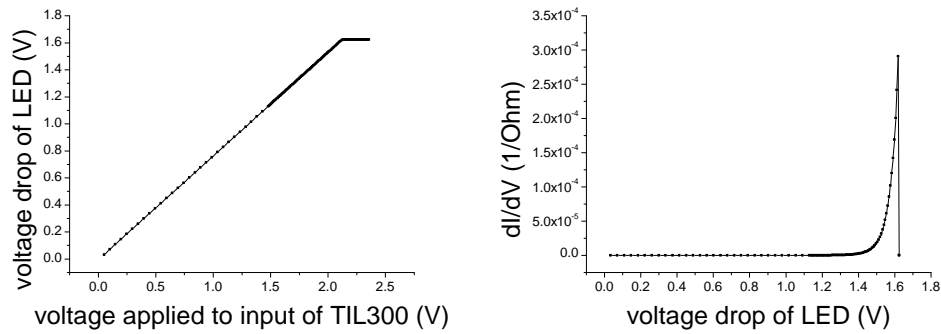
Figure 4.14: Left: voltage drop of the LED as a function of input voltage of the TIL300 circuit, recorded at the same time as the right figure. Right: Results of differential conductance measurements of the LED.
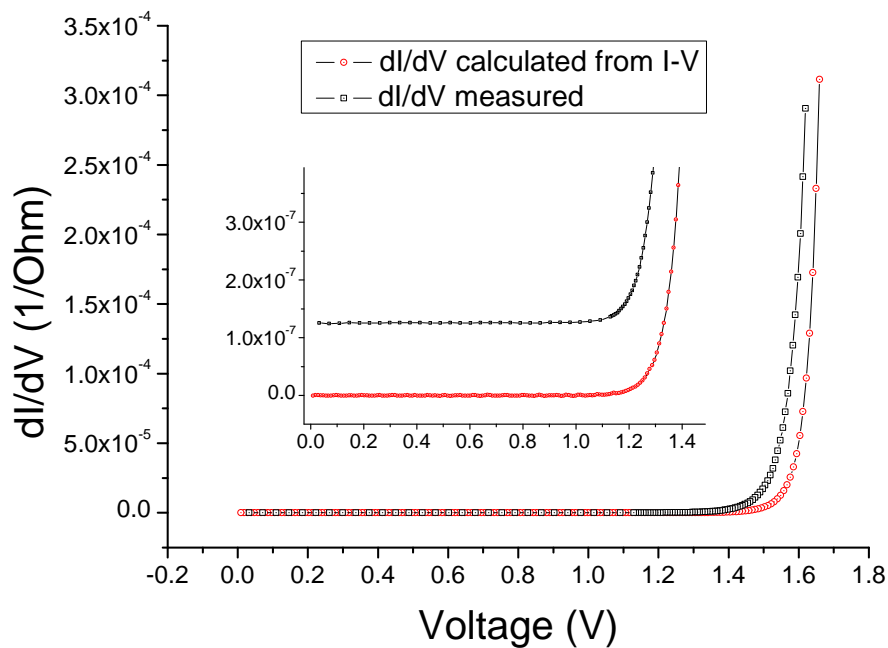
Figure 4.15: Black curve is the directly measured differential conductance of the LED. Red curve is the differential conductance of the LED calculated by numerically differentiating the I-V curve. Inset shows an enlarged figure of the low-bias region.

Fig 4.15 shows a comparison of the measured differential conductance result with the result numerically differentiated from the I-V curve. Roughly the two results are consistent with each other. The inset of Fig 4.15 shows

a relatively large difference between the two results at bias voltages far less than the turn-on voltage of the LED. The calculated result is $\sim 10^{-10}\Omega^{-1}$, while the measured result is $\sim 10^{-7}\Omega^{-1}$. The reason might be that when the conductance of the LED is very small, the ac current is too small to be detected by the lock-in amplifier. And the ac current measured is actually a constant noise signal.

4.3.6   Summary

We spent quite a lot of time on developing the DRMS. Although there are still some problems we are not clear about, the setup can work well if we carefully run the experiment. Fig 4.15 shows a not bad consistency between measured differential conductance of an LED and that calculated from I-V data. We believe that, if we make a neater circuit and do some further improvements, we'll get a better result. After all, the circuit we are presently using, as show in Fig 4.6, is just one for preliminary test. A possible improvement might be to introduce the Adler-Jackson bridge, as described in Ref [25] and [30]. Anyway, so far we've established a well-working DRMS. So we decided to do some test measurements on point contacts.

4.4   Tip and sample preparation

4.4.1   Tip preparation

Fig 4.16 is the Scanning Electron Microscope (SEM) picture of the sharp tungsten (W) tip prepared by electrochemical etching. A W wire of $50\mu m$ diameter is used here. From Fig 4.16 we can see that the diameter of the tip is less than $1\mu m$. Ref [11] mentions that a good ("Good" means exhibiting the greatest range of I-V curve characteristics here.) tip for experiments is slightly more concave than a simple cone shape. Our tip satisfies this criterion.
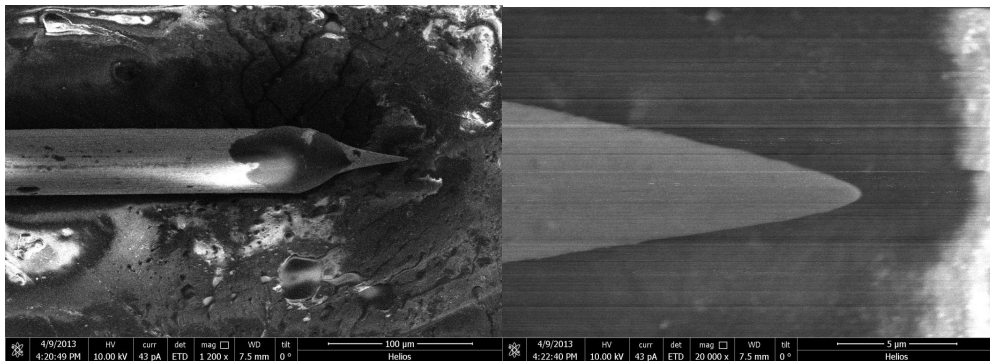
Figure 4.16: SEM pictures of tungsten tip prepared by electrochemical etching.

4.4.2   The Ti/Au sample

A simple Ti/Au sample (Ti $\sim$2nm, Au $\sim$20nm) is prepared by thermal evaporation on a Si substrate. Aluminum wires are used for wire bonding. Fig 4.17 shows optical microscopic images of the sample.
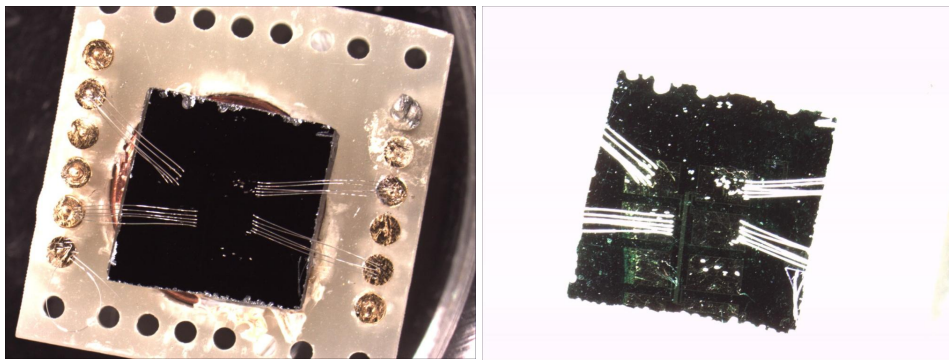

Figure 4.17: Optical microscopic pictures of the Ti/Au sample after wire bonding.

4.4.3   The YBCO sample

Fig 4.18 shows optical microscopic images of the YBCO sample ($\sim$200nm). Four Ti/Au (Ti $\sim$2nm, Au $\sim$20nm) pads are thermal evaporated on YBCO as electrodes. Aluminum wires are used for wire bonding.
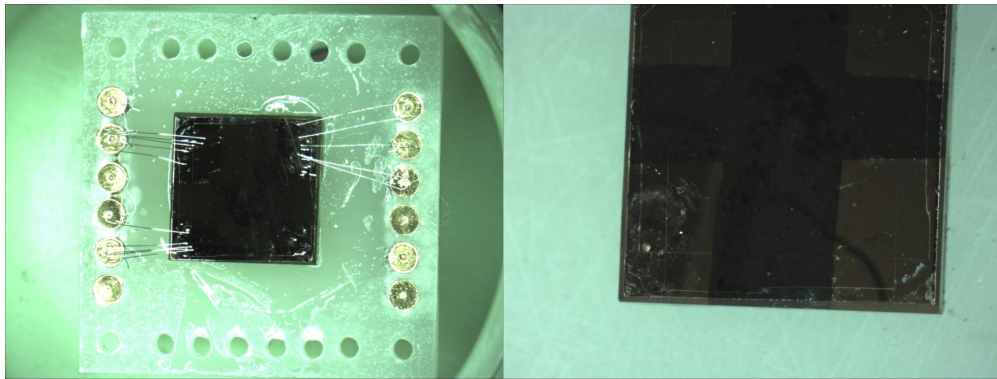
Figure 4.18: Optical microscopic pictures of the YBCO sample after wire bonding.

4.5   Sample holder and wirings

4.5.1   The overall wiring configuration

Fig 4.19 shows the overall wiring configuration for our experiments. A W tip is attached to one of the two arms of the tuning fork. A gold wire is connected to the tip. When a point contact is formed between the W tip and the sample, current will flow through the sample to the tip and the gold wire; and voltage will be measured between the tip (actually the gold wire) and the sample. So this is a pseudo four-wire method (only three terminals). It's difficult to attach two separate gold wires to the tip.

Fig 4.19 also shows the sample holder, which could be easily mounted on the piezo stack of the AFM.

4.5.2   Procedure for connecting a gold wire to the tip

Following is a standard procedure we used to connect a gold wire to the tungsten tip.

1. Solder the TF to the PCB. See Fig 4.20. Note that the two copper wires in Fig 4.20 represent the two electrodes from the TF coax, which are

soldered beforehand. Another copper wire is also soldered beforehand, which will be finally connected to the gold wire.
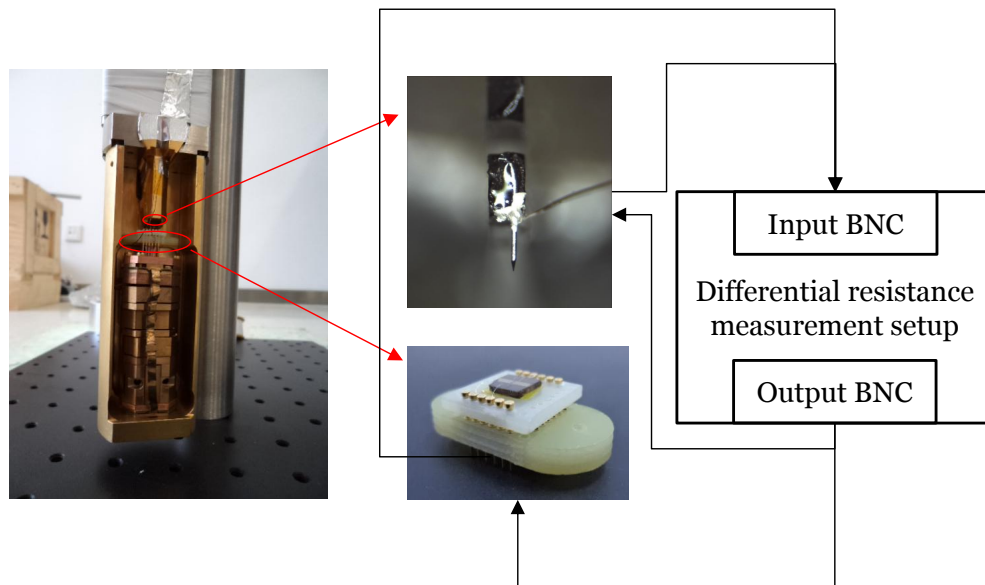

Figure 4.19: Overall wiring configuration of our point contact experiments. Cf. Fig 4.7
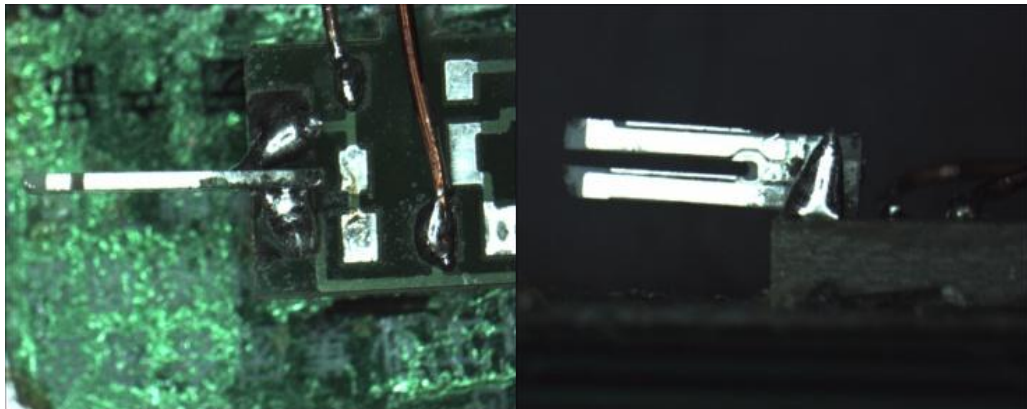
Figure 4.20: Procedure for connecting a gold wire to the tip - solder the TF to the PCB.

2. Attach the W tip to one of the two arms of the TF. See left figure of Fig 4.21.

3. Tie the gold wire to the W tip. See right figure of Fig 4.21.
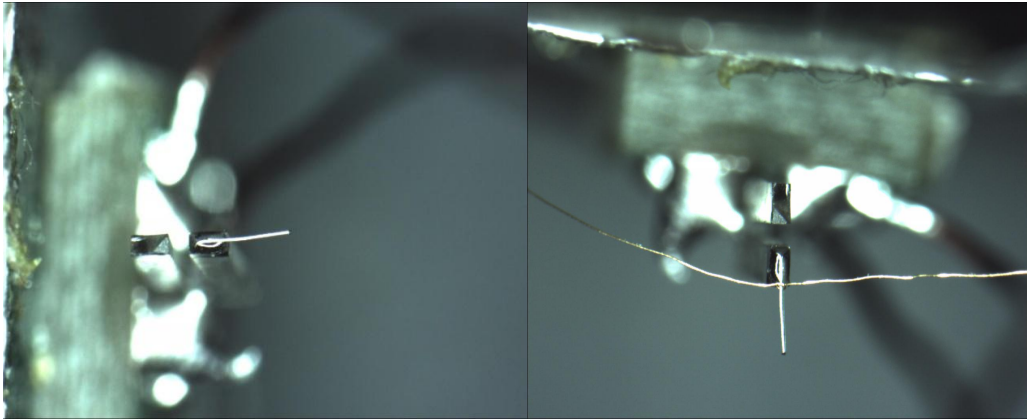
Figure 4.21: Procedure for connecting a gold wire to the tip - attach the tip and tie the gold wire.

4. Put one drop of silver paint at the connecting part. I used an eyelash to attach the silver paint. See Fig 4.22.
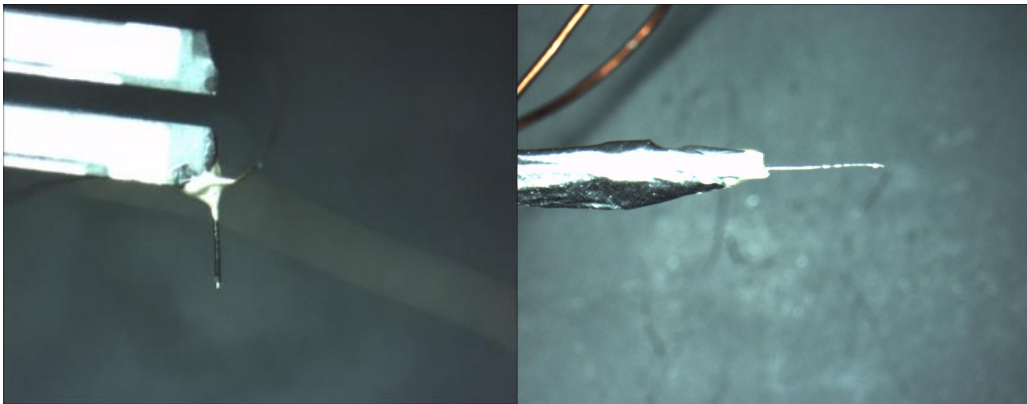

Figure 4.22: Procedure for connecting a gold wire to the tip - connect the tip and the wire with silver paint.

5. Finally, attach the gold wire to the PCB. The final configuration should be like Fig 4.23.
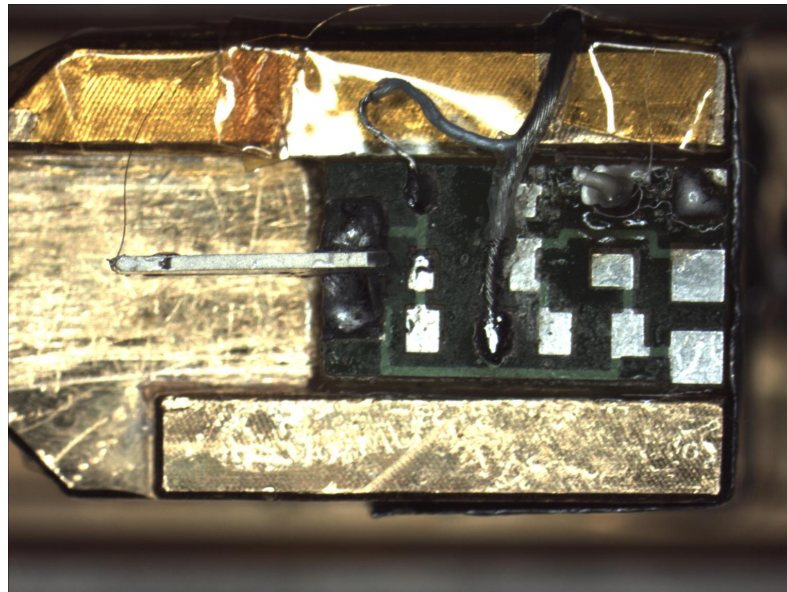
Figure 4.23: Procedure for connecting a gold wire to the tip: final configuration.

Chapter 5

Results

5.1 Procedure for a dV/dI measurement

Following is a standard procedure for our differential resistance measurements of point contacts.

1. Mount the sample on the piezo stack of the AFM and make sure the wirings are all right.

2. Do some locating work. Since we will not know the tip position relative to the sample at low temperature, we need to write down the x and y positions of the target point.

3. Try auto-approaching and make sure that tuning fork, positioners and scanners all work well.

4. Put the AFM insert into the vacuum tube and vacuumize it. We usually leave $\sim$10mbar helium gas as exchange gas.

5. Put the insert into liquid nitrogen and simultaneously monitor the resistance of the sample. (For the YBCO sample, we should observe a superconducting transition.)

6. Prepare the DRMS. Make sure every battery is fully charged. (I will not use a battery of voltage less than 11.5V.) Make sure DRMS works

well.

7. Measure the output voltage of the TIL300 circuit as a function of the input voltage of it. This is useful for data processing.

8. When temperature is low enough, we can start making the point contact. First use auto-approach of the AFM. When auto-approach finished, turn off the excitation voltage of the tuning fork, because from now on we do not want the tuning fork to oscillate. Start monitoring the resistance of the contact. (It should be OL now.) Then carefully approach the sample to the tip manually. When the resistance starts to be some not-overloaded value, we can change to smaller approaching steps. When a stable contact is formed (The resistance of it does not drift much with time.), differential resistance measurements could be started.

5.2   Results for W tip on Ti/Au sample

5.2.1   Results at room temperature (RT)

We first did some tests at RT using a W tip and a Ti/Au sample. Fig 5.1 shows the results. The point contact resistance is about 11Ω. A current bias method is employed, with an $R_{v2i} = 1k\Omega$. The ac current is 77Hz and about $10\mu A$. DC bias current is from 0 to about 10mA. From Fig 5.1 we can see that the measured value of differential resistance is indeed reasonable, although repeatability is not good. This is because when at RT and exposed into air, the contact is sensitive to environmental vibrations and not stable. We can see this effect from the R vs dc bias voltage curve in Fig 5.1 (the right figure). Also, there are some weird anomalies in the differential resistance curves, which turn out to be resulted from problems in the circuit of DRMS. We finally get rid of these anomalies after some struggling. Note

that we've only got screenshots of these results because of some problems of the LabVIEW programs at that time.
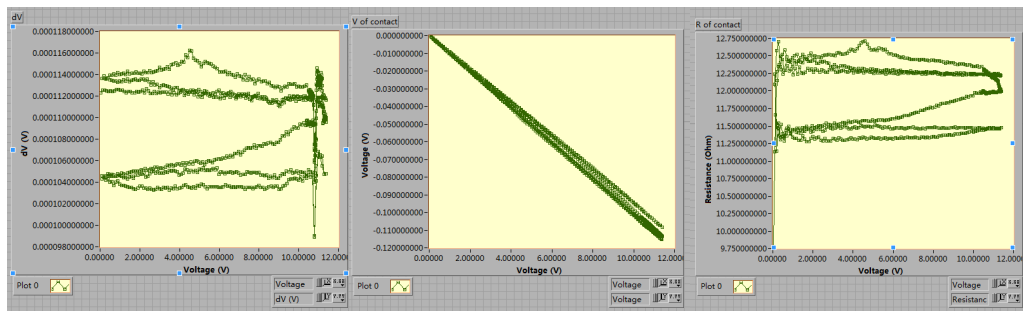

Figure 5.1: Results of differential resistance measurements (three times back and forth) of a W-Ti/Au point contact at RT.

5.2.2 Results at 77K

Fig 5.2 shows results of a W tip on a Ti/Au sample at 77K. The contact resistance is about 5Ω. The ac current is 117Hz and about $1\mu A$. DC bias current is from 0 to about 10mA. The following points can be concluded from the results.

- There are no clear structures within the noise level.

- Fig 5.2 shows results of a back and forth measurement. It can be seen that at low temperature (LT) and vacuum the repeatability is much better, because the point contact is more stable.

- There is a $\sim 0.5\mu V$ white noise in the readout of the lock-in amplifier, regardless of ac frequency or amplitude. We are not clear about its origin. It might be some noise generated from the DRMS circuit. This noise corresponds to a $\sim 20m\Omega$ fluctuation in the differential resistance data. Fig 3 (b) of Ref [31] shows a fluctuation of about $\sim 15m\Omega$, similar to our results.

- By appropriately enlarge the ac amplitude and match R_{v2i} with the contact resistance, high resolution of dV/dI could be achieved: 1% structures could be clearly distinguished.
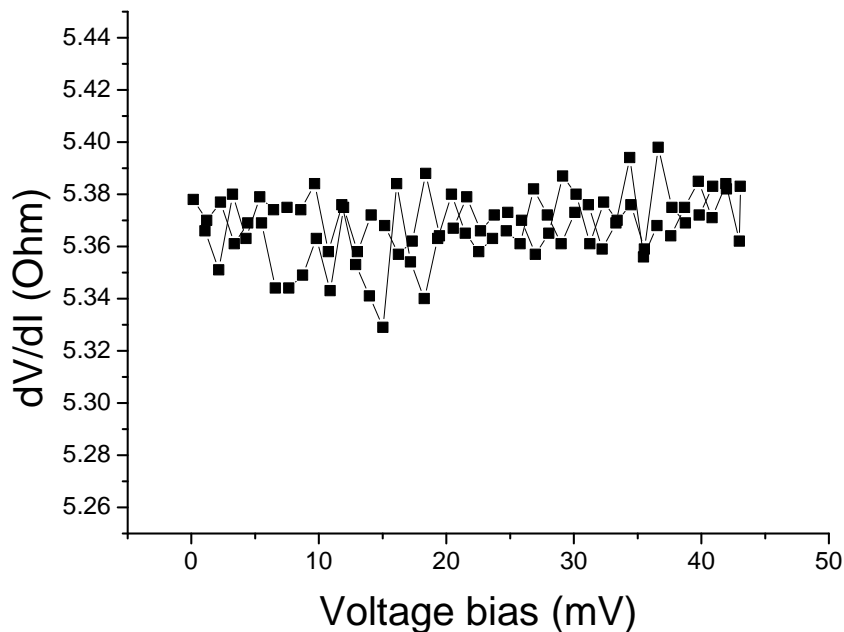

Figure 5.2: Results of differential resistance measurements (back and forth) of a W-Ti/Au point contact at 77K.

5.3 Results for W tip on YBCO sample

In this section we discuss the results of differential resistance measurements for a W tip on a YBCO sample. Fig 5.3 shows the superconducting transition of our YBCO sample. The large resistance in the superconducting region is due to our two-wire method for resistance measurement. We just want to make sure that the sample is indeed superconducting at 77K.

Because of the tight schedule, we do not have enough time to get a good differential resistance result. Fig 5.4 shows a really bad result we've got (which is also the best one we've got). The seemingly step at ∼50-60mV dc bias voltage might be a signature of the gap structure of YBCO.
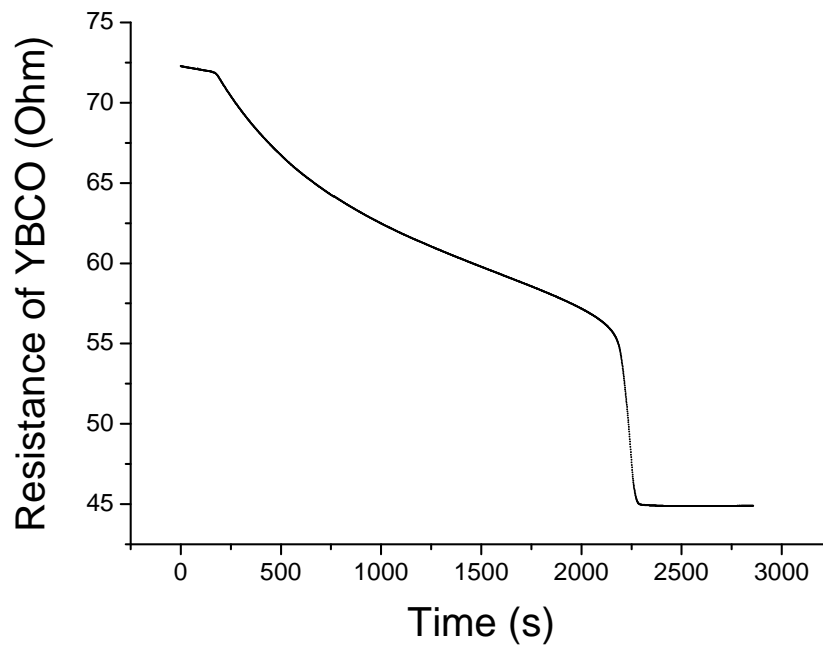
Figure 5.3: Superconducting transition of the YBCO sample.

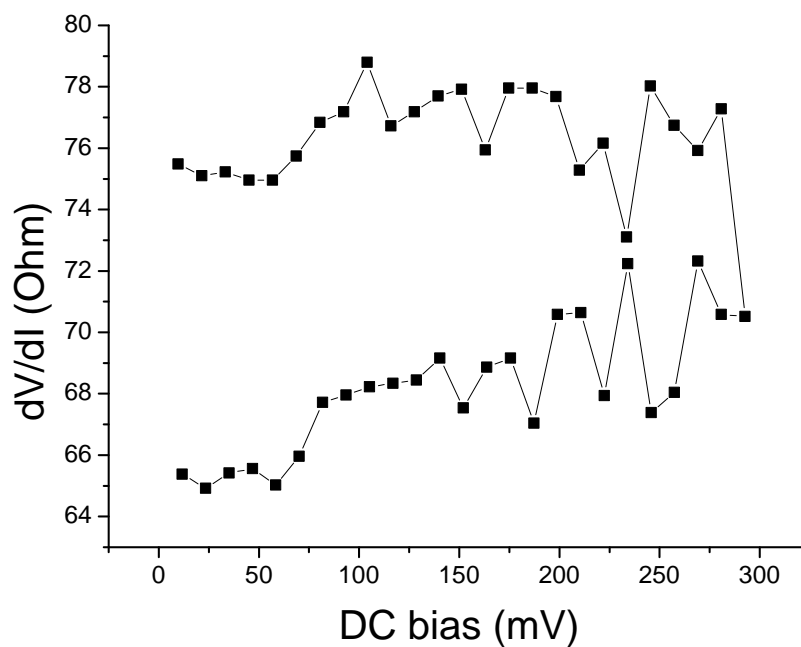Figure 5.4: Results of differential resistance measurements (back and forth) of a W-YBCO point contact at 77K.

Chapter 6

Concluding remarks

We have established a PCARS experiment setup based on an Attocube low temperature AFM and obtained differential resistance curves of W-Ti/Au and W-YBCO point contacts. The stability of the setup and resolution of the measurement still need to be improved.

Bibliography

[1] Jian Wei. Research summary. `http://millikelvin.pku.edu.cn/research/WEI_Research.html`, April 2011.

[2] H.van Houten. Quantum point contacts. *Physics Today*, page 22, July 1996.

[3] G.E.Blonder et al. Transition from metallic to tunneling regimes in superconducting microconstrictions: Excess current, charge imbalance, and supercurrent conversion. *Phys.Rev.B*, 25:4515, 1982.

[4] P.G.de Gennes. Boundary effects in superconductors. *Rev.Mod.Phys*, 36:225, 1964.

[5] J.Linder et al. Spin-active interfaces and unconventional pairing in half-metal/superconductor junctions. *Phys.Rev.B*, 81:174526, 2010.

[6] Matthias Eschrig. Spin-polarized supercurrents for spintronics. *Phys.Today*, 64:43–49, 2011.

[7] G.Deutscher. Andreev-Saint-James reflections: A probe of cuprate superconductors. *Rev.Mod.Phys*, 77:109–135, 2005.

[8] A.Andreev. . *Sov.Phys.JETP*, 19:1228, 1964.

[9] Xin Lu. Point-contact Andreev reflection studies on superconductors. PhD Thesis of University of Illinois Urbana Champaign, 2010.

[10] D.Daghero et al. Strong-coupling d-wave superconductivity in $PuCoGa_5$ probed by point-contact spectroscopy. *Nature Communications*, 3(4):786, 2012.

[11] G.E.Blonder et al. Metallic to tunneling transition in Cu-Nb point contacts. *Phys.Rev.B*, 27(1):112–118, 1983.

[12] A.I.Buzdin. Proximity effect in superconductor-ferromagnet heterostructures. *Rev.Mod.Phys*, 77:935–975, 2005.

[13] F.S.Bergeret et al. Odd triplet superconductivity and related phenomena in superconductor-ferromagnet structures. *Rev.Mod.Phys*, 77:1321–1373, 2005.

[14] R.J.Soulen Jr. et al. Measuring the spin polarization of a metal with a superconducting point contact. *Science*, 282:85–88, 1998.

[15] M.Wimmer et al. Quantum point contact as a probe of a topological superconductor. *New Journal of Physics*, 13:053016, 2001.

[16] C.W.J.Beenakker. Search for Majorana fermions in superconductors. *arXiv:1112.1950v2*, 2011.

[17] T.M.Klapwijk. Proximity effect from an Andreev perspective. *J. Supercond. Novel Magn.*, 17(5):593–611, 2004.

[18] C.Visani et al. Equal-spin Andreev reflection and long-range coherent transport in high-temperature superconductor/half metallic ferromagnet junctions. *Nature Physics*, 8:539–543, 2012.

[19] I.Fridman et al. Scanning tunneling spectroscopy study of c-axis proximity effect in epitaxial bilayer manganite/cuprate thin films. *Phys.Rev.B*, 84:104522, 2011.

[20] Y.Kalcheim et al. *Phys.Rev.B*, 83:064510, 2011.

[21] T.Lofwander et al. Shot noise in normal metal-d-wave superconducting junctions. *Phys.Rev.B*, 68:054504, 2003.

[22] J.A.Celis et al. Shot noise in HTc superconductor quantum point contact system. *arXiv:1210.5019v1*, 2012.

[23] P.Romano et al. Non-monotonic behavior of the superconducting order parameter in Nb/PdNi bilayers observed through point contact spectroscopy. *arXiv:1207.1879*, 2012.

[24] Yu.G.Naidyuk et al. Point-contact spectroscopy. *arXiv:physics/0312016v1*, 2003.

[25] Jose Aumentado. Nonequilibrium and quantum transport phenomena in mesoscopic ferromagnet/superconductor heterostructures. PhD Thesis of Northwestern University, 2000.

[26] Chen-Jung Chien. Transport phenomena near the normal-metal/superconducting interface in mesoscopic devices. PhD Thesis of Northwestern University, 1998.

[27] Jian Wei. Summary of noise measurements for SIN sample 20090422. 2009.

[28] Texas Advanced Optoelectronic Solutions. Data sheet of precision linear optocoupler TIL300. 1999.

[29] Ametek Signal Recovery. Model 7265 DSP lock-in amplifier instruction manual. 2002.

[30] J.G.Adler et al. System for observing small nonlinearities in tunnel junctions. *Rev.Sci.Instrum*, 37(8):1049–1054, 1966.

[31] P Cadden-Zimansky et al. Coherent nonlocal correlations in Andreev interferometers. *New Journal of Physics*, 14:043004, 2012.

毕 业 论 文（设计） 考 核

一、指导教师对毕业论文（设计）的评语：

指导教师(签名)

年 月 日

二、答辩小组对毕业论文（设计）的答辩评语及总评成绩：

成 绩比例	文献综述占（10%）	开 题 报告占（20%）	外 文 翻译占（10%）	毕业论文（设计）质量及答辩占（60%）	总 评成绩
分值					

答辩小组负责人（签名）

年 月 日